



Cite this: *J. Mater. Chem. A*, 2025, **13**, 19923

## Unveiling the structural and magnetic properties of $\text{RENaGeO}_4$ (RE = Gd, Dy, and Ho) oxides and remarkable low-temperature magnetocaloric responses in $\text{GdNaGeO}_4$ oxide

Yikun Zhang, \* Yingzhe Na, Yang Xie and Xinyu Zhao

Low-temperature magnetocaloric (MC) responses in various types of solid-state magnets have been extensively determined, with the aim of developing high-performing MC materials for magnetic refrigeration applications and deepening our understanding of their underlying intrinsic magneto-physical characteristics. Herein, we fabricated a family of single-phase rare-earth (RE)-dominated oxides, namely,  $\text{RENaGeO}_4$  (RE = Gd, Dy, and Ho), by applying the solid phase reaction method and unveiled their structural and magnetic properties, specifically to low-temperature MC responses through experimental determination and theoretical calculation. All  $\text{RENaGeO}_4$  oxides crystallize in an orthorhombic olivine-type structure with the space group *Pnma* (No. 62) and order magnetically at temperatures of 0.70, 2.28, and 2.15 K for  $\text{GdNaGeO}_4$ ,  $\text{DyNaGeO}_4$ , and  $\text{HoNaGeO}_4$  oxides, respectively. The consistent elements in these  $\text{RENaGeO}_4$  oxides are distributed uniformly and present as  $\text{RE}^{3+}$ ,  $\text{Na}^{1+}$ ,  $\text{Ge}^{4+}$ , and  $\text{O}^{2-}$  valence states. The low-temperature MC responses in these  $\text{RENaGeO}_4$  oxides are identified by the MC parameters of maximum magnetic entropy change and relative cooling power. These MC parameters under magnetic field changes ( $\Delta\mu_0H$ ) of 0–2/0–5 T are as follows: 34.98/47.30 J (kg K)<sup>-1</sup> and 107.56/320.70 J kg<sup>-1</sup> for  $\text{GdNaGeO}_4$ , 11.23/14.82 J (kg K)<sup>-1</sup> and 77.70/236.82 J kg<sup>-1</sup> for  $\text{DyNaGeO}_4$ , and 12.21/15.37 J (kg K)<sup>-1</sup> and 81.18/239.47 J kg<sup>-1</sup> for  $\text{HoNaGeO}_4$ . Evidently, these determined MC parameters for  $\text{GdNaGeO}_4$  oxide, especially under relatively low  $\Delta\mu_0H$ , are much larger than those for the commercial MC material of  $\text{Gd}_3\text{Ga}_5\text{O}_{12}$  oxide and surpass those of most updated benchmarked low-temperature MC materials, making the  $\text{GdNaGeO}_4$  oxide an excellent candidate for low-temperature magnetic refrigeration application.

Received 4th February 2025  
Accepted 14th May 2025

DOI: 10.1039/d5ta00892a

rsc.li/materials-a

## Introduction

Solid-state magnetic refrigeration,<sup>1–4</sup> which leverages the magnetocaloric (MC) effect in solid-state magnets, is a distinct and prospective low-temperature cooling method<sup>3–8</sup> owing to its notable economic and environmental benefits. The MC effect, recognized as an inherent magneto-physical property of all solid-state magnets,<sup>1–8</sup> can be primarily accessed through the change in magnetic entropy ( $\Delta S_{\text{M}}^{\text{max}}$ ) under a fixed change in the magnetic field ( $\Delta\mu_0H$ ). However, the development of practical magnetic refrigeration applications has been hindered by the lack of high-performing MC materials.<sup>3–8</sup> Thus, various types of solid-state magnets<sup>4–16</sup> have been fabricated and extensively determined regarding their MC responses over the last three decades, with the aim of exploring high-performing MC materials for practical refrigeration applications<sup>4–24</sup> and better understanding their underlying intrinsic magneto-physical

characters.<sup>6–18</sup> Consequently, several high-performance MC materials capable of operating at various temperature ranges have been achieved,<sup>3–18</sup> such as  $(\text{Mn, Fe})_2(\text{P, X})$ ,  $\text{Gd}_5(\text{Si, Ge})_4$ ,  $\text{La}(\text{Fe, Si})_{13}\text{H}_y$ ,  $\text{Ni}_2\text{MnX}$ ,  $\text{Mn}_{30}(\text{Fe, Cu})_{20}\text{Al}_{50}$ , and some rare earth (RE)-dominated solid-state magnets.

Among the array of achieved high-performing low-temperature MC materials, rare-earth (RE)-dominated magnetic solids<sup>12–26</sup> account for the highest proportions. For example, pure or partially doped RE(Co, Ni)<sub>2</sub> Laves-phase compounds<sup>18–21</sup> have recently been reported to possess remarkable MC responses, which are considerable for hydrogen liquification applications. A large low-temperature MC effect in  $\text{A}_2\text{GdSbO}_6$  oxides was reported by Koskelo *et al.*,<sup>22</sup> which correlates with their free-spin dominant magnetic behaviors.<sup>22</sup> Remarkable low-temperature MC responses were very recently reported in  $\text{Gd}_2\text{Ti}_2\text{O}_7$  and  $\text{SrGd}_2\text{O}_4$  oxides,<sup>23,24</sup> which correlate with their geometrically frustrated magnetic structure.<sup>23,24</sup> The  $\text{Er}_{1-x}\text{Tm}_x\text{Ga}$  compounds were fabricated by Wang *et al.*,<sup>25</sup> which are reported to possess large MC responses around hydrogen liquification temperature. The low-temperature MC effects in

School of Electronics and Information, Hangzhou Dianzi University, Hangzhou 310012, China. E-mail: ykzhang@hdu.edu.cn

RE(OH)<sub>3</sub> compounds have recently been characterized, and Dy(OH)<sub>3</sub> was observed to be a high-performing low-temperature MC material.<sup>26</sup> Enhanced low-temperature MC responses were recently achieved in Gd<sub>2</sub>CuTiO<sub>6</sub> and GdCoC compounds,<sup>27,28</sup> which are governed by 4f-3d magnetic ground state interactions. The low-temperature MC effects of RE<sub>2</sub>CoTiO<sub>6</sub> oxides<sup>29</sup> were investigated, and remarkable MC responses were achieved in Gd<sub>2</sub>CoTiO<sub>6</sub> oxide.<sup>29</sup> These results collectively indicate that numerous unknown RE-dominated magnetic solids hold high potential as high-performing low-temperature MC materials, warranting our in-depth investigation.

Additionally, extensive investigations have been performed on RE-dominated magnetic oxides<sup>22–24,27–30</sup> owing to their benefits of being easy to fabricate and good environmental stability. Thus, we herein shift our research interest to RENaGeO<sub>4</sub> oxides,<sup>31–36</sup> which have attracted research interest recently owing to their significant potential as luminescent phosphors.<sup>33–36</sup> However, a detailed investigation of RENaGeO<sub>4</sub> oxides on their magnetic properties and MC responses is still lacking. Therefore, building on our previous studies<sup>27–30</sup> focused on developing high-performing low-temperature MC materials and deepening our understanding of the inherent magneto-properties of RENaGeO<sub>4</sub> oxides, in this work, we fabricated three polycrystalline oxides of GdNaGeO<sub>4</sub>, DyNaGeO<sub>4</sub>, and HoNaGeO<sub>4</sub> and unveiled their structural and magnetic properties, specifically their cryogenic MC responses experimentally and theoretically. Our studies indicate that GdNaGeO<sub>4</sub> oxide possesses remarkably low-temperature MC responses, especially under relatively low  $\Delta\mu_0H$ , which is an exceptionally promising candidate for practical refrigeration applications.

## Experimental and calculation details

Three polycrystalline samples of GdNaGeO<sub>4</sub>, DyNaGeO<sub>4</sub> and HoNaGeO<sub>4</sub> were fabricated by applying the method of solid phase reaction using raw materials of Gd<sub>2</sub>O<sub>3</sub>/Dy<sub>2</sub>O<sub>3</sub>/Ho<sub>2</sub>O<sub>3</sub>, Na<sub>2</sub>CO<sub>3</sub> and GeO<sub>2</sub> powders (purity all exceeding 99.9 wt.%). First, stoichiometric amounts of these oxide powders were weighed, hand-mixed and carefully ground. Second, the thoroughly mixed and ground powders were placed in a muffle furnace at 950 °C for 26 hours. Third, the resulting products were reground into fine powders and directly pelleted by cold pressing. Finally, the dense GdNaGeO<sub>4</sub>, DyNaGeO<sub>4</sub> and HoNaGeO<sub>4</sub> oxides were acquired by the final thermal treatment of these pellets at 1020 °C, 1120 °C and 1170 °C for 50 hours, respectively.

The phase and structural properties of RENaGeO<sub>4</sub> oxides are assessed by applying a Rigaku X-ray diffractor (XRD, SmartLab). The element distributions and microstructure of RENaGeO<sub>4</sub> oxides were characterized by selective area electron diffraction (SAED), transmission electron microscopy (TEM, FEI-Talos-F200s) and attached energy dispersive spectroscopy (EDS). The valence states in RENaGeO<sub>4</sub> oxides were accessed by Thermo Scientific X-ray photoelectron spectroscopy (XPS, K-Alpha) utilizing C-1s as the reference energy. The magnetization measurements of RENaGeO<sub>4</sub> oxides were performed by applying

a quantum design magnetic property measurement system (MPMS-Q3) with a magnetic field and temperature sweep rates of 30 mT s<sup>-1</sup> and 3 K min<sup>-1</sup>, respectively. The magnetization results of GdNaGeO<sub>4</sub> below 1.8 K were obtained using a dilute He-3 refrigerator with magnetic field and temperature sweep rates of 10 mT s<sup>-1</sup> and 0.3 K min<sup>-1</sup>, respectively.

Atomic-level first-principles electronic and magnetic structure calculations of RENaGeO<sub>4</sub> oxides were conducted within the framework of spin-polarized density functional theory (DFT).<sup>37–39</sup> The calculations utilized the commercial Vienna *ab initio* Simulation Package (VASP) software, employing plane waves with a cutoff energy of 520 eV to reproduce the one-electron wave function for constructing the basis set and projected augmented waves (PAW) pseudopotentials.<sup>37–39</sup> The valence electron states in PAW pseudopotentials of Gd [4f<sup>7</sup> 5s<sup>2</sup> 5p<sup>6</sup> 5d<sup>1</sup> 6s<sup>2</sup>], Dy [4f<sup>10</sup> 5s<sup>2</sup> 5p<sup>6</sup> 6s<sup>2</sup>], Ho [4f<sup>11</sup> 5s<sup>2</sup> 5p<sup>6</sup> 6s<sup>2</sup>], Na [2s<sup>2</sup> 2p<sup>6</sup> 3s<sup>1</sup>], Ge [3d<sup>10</sup> 4s<sup>2</sup> 4p<sup>2</sup>], and O [2s<sup>2</sup> 2p<sup>4</sup>] were considered in RENaGeO<sub>4</sub> oxides explicitly during the calculations. The *k*-space integrations during calculation were set as 3 × 5 × 6 using the Monkhorst–Pack method.<sup>37–39</sup> Structural optimizations of RENaGeO<sub>4</sub> oxides were conducted using a conjugate gradient algorithm until each self-consistent electronic loop and the Hellman–Feynman forces converged to below 10<sup>-7</sup> eV per atom and -0.01 eV Å<sup>-1</sup>, respectively.

## Results and discussion

We first assessed the phase and structural characters of RENaGeO<sub>4</sub> (RE = Gd, Dy, and Ho) oxides by XRD at room temperature (RT) and Rietveld structural refinement utilizing the Fullprof suite.<sup>40</sup> The resulting experimental and refined XRD patterns of GdNaGeO<sub>4</sub>, DyNaGeO<sub>4</sub>, and HoNaGeO<sub>4</sub> oxides are illustrated in Fig. 1(a)–(c), respectively. All the diffraction peaks of these RENaGeO<sub>4</sub> oxides could be indexed and well-fitted to an orthorhombic Olivine-type structure (*Pnma* space group, No. 62). The values of fitted reliability parameters, including  $R_b$ ,  $R_{wp}$  and  $R_{exp}$ , are as follows: 3.48%, 4.60% and 2.21% for GdNaGeO<sub>4</sub>; 3.63%, 5.01% and 1.98% for DyNaGeO<sub>4</sub>; and 4.05%, 6.89% and 1.67% for HoNaGeO<sub>4</sub>; respectively. These parameters are reasonably low, indicating the reliability of the present fitting and good matching with a structural model. Additionally, the refined lattice parameters *a*, *b*, *c* and *V* are 11.5487(15), 6.5334(9), 5.3012(7) Å and 399.984 Å<sup>3</sup> for GdNaGeO<sub>4</sub>; 11.4400(17), 6.4839(9), 5.2764(8) Å and 391.378 Å<sup>3</sup> for DyNaGeO<sub>4</sub>; and 11.4167(21), 6.4488(12), 5.2748(11) Å and 388.353 Å<sup>3</sup> for HoNaGeO<sub>4</sub>, respectively, in which all decrease monotonically with increasing atom number of RE ions, as illustrated in Fig. 1(d), aligned well with the contraction principle of RE elemental. The schematic structural diagrams of RENaGeO<sub>4</sub> oxides are illustrated in Fig. 2. Generally, the RE, Na, and Ge atoms in RENaGeO<sub>4</sub> oxides are coordinated with six, six, and four O atoms and form irregular REO<sub>6</sub> octahedra, NaO<sub>6</sub> octahedra, and GeO<sub>4</sub> tetrahedra, respectively. The REO<sub>6</sub> and NaO<sub>6</sub> octahedra exhibit similar behavior, sharing two O atoms with themselves and forming octahedral chains along the *a*-axis. Within the *bc*-plane, the NaO<sub>6</sub> octahedra are corner shared with four equivalent REO<sub>6</sub> octahedra and two equivalent GeO<sub>4</sub>

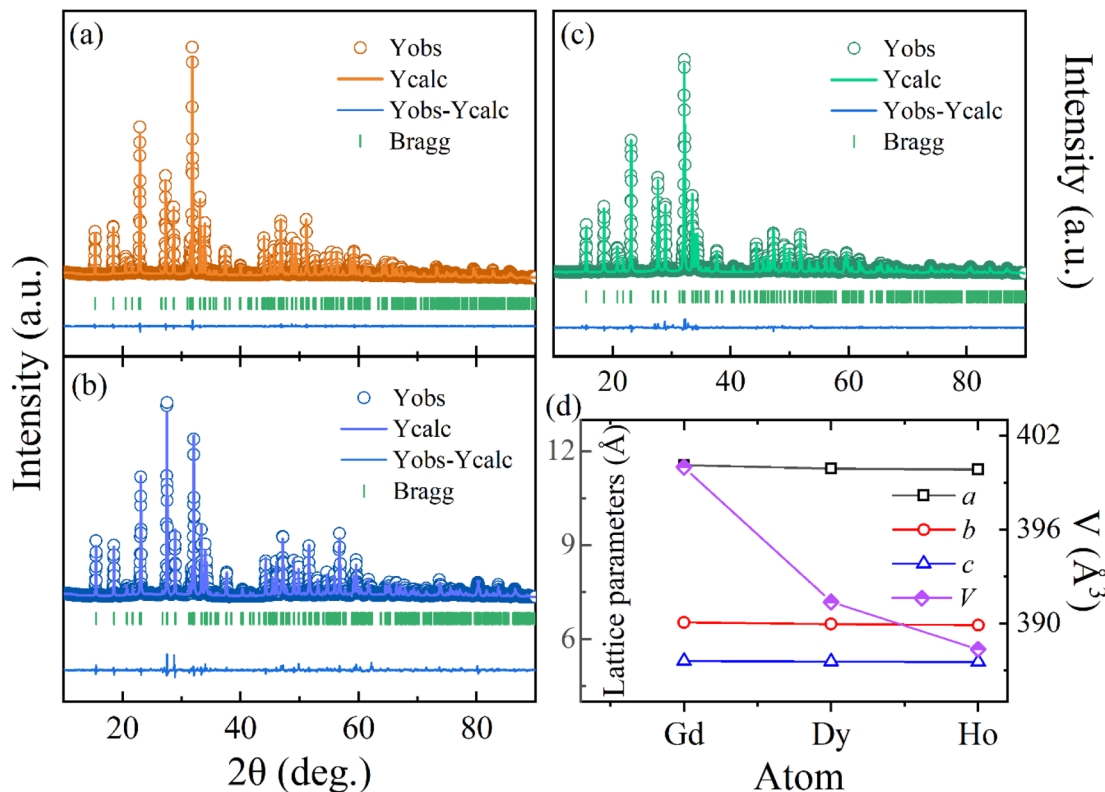


Fig. 1 Experimental and calculated XRD patterns of (a) GdNaGeO<sub>4</sub>, (b) DyNaGeO<sub>4</sub>, and (c) HoNaGeO<sub>4</sub> oxides. (d) Lattice parameter (*a*, *b*, *c*, and *V*) variations of RENaGeO<sub>4</sub> oxides.

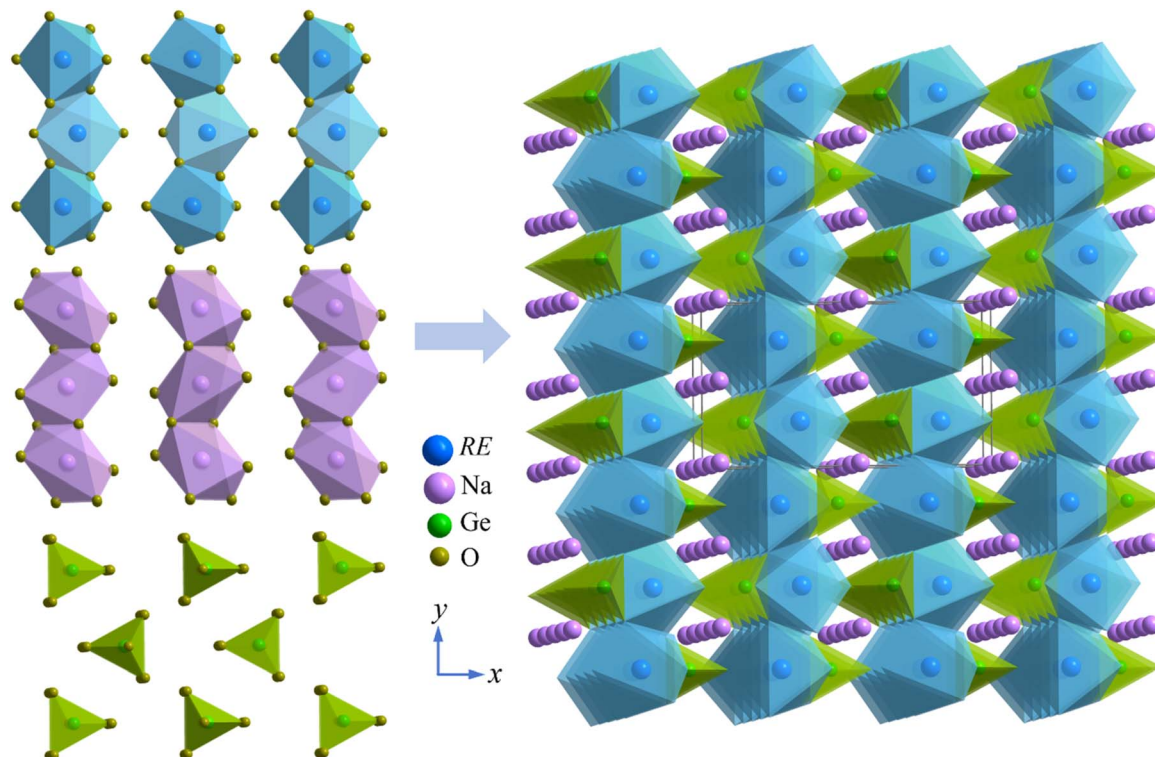


Fig. 2 Schematic of RENaGeO<sub>4</sub> oxides.

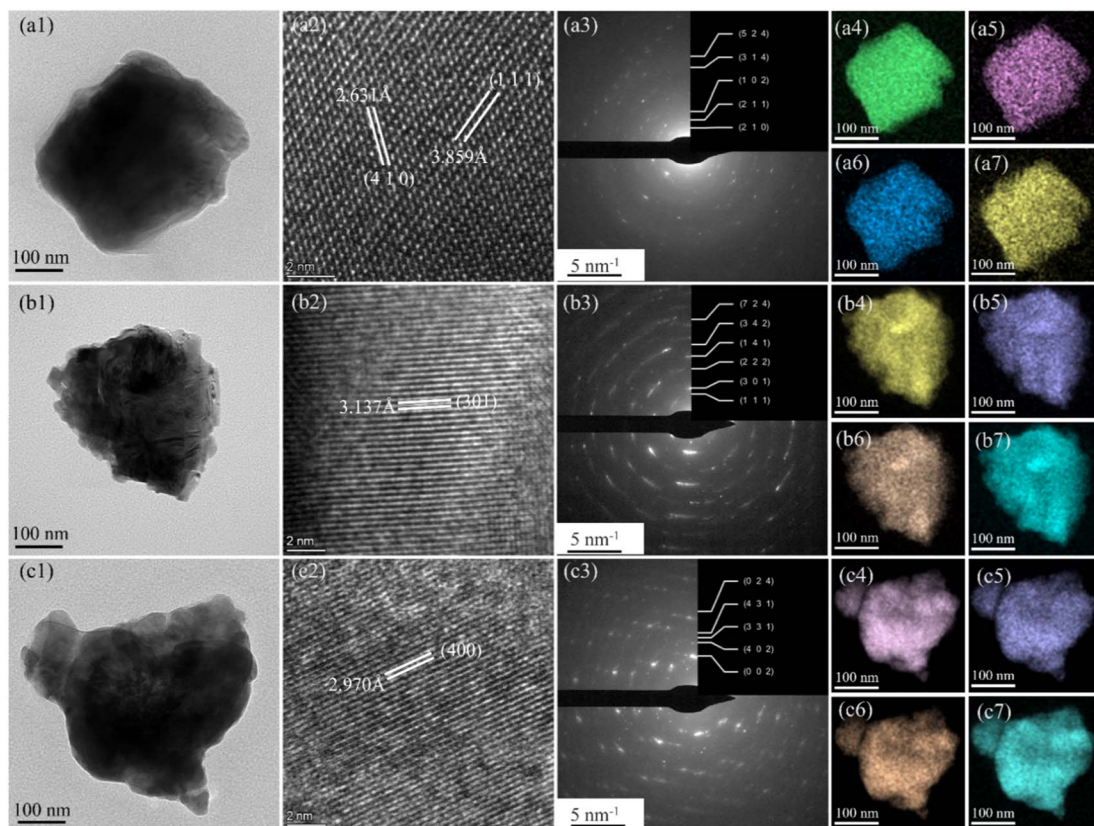


Fig. 3 TEM, SAED, and EDS results of (a1–a7)  $\text{GdNaGeO}_4$ , (b1–b7)  $\text{Dy}_2\text{NaGeO}_4$ , and (c1–c7)  $\text{HoNaGeO}_4$  oxides.

tetrahedra; it is also edge shared with two equivalent  $\text{REO}_6$  octahedra and  $\text{GeO}_4$  tetrahedron, resulting in a quasi-two-dimensional (2D) structural character of  $\text{RENaGeO}_4$  oxides.

The bright-field TEM images and corresponding fast Fourier transforms of  $\text{GdNaGeO}_4$ ,  $\text{DyNaGeO}_4$  and  $\text{HoNaGeO}_4$  oxides are illustrated in Fig. 3. The plane spacings of  $\text{GdNaGeO}_4$  oxide

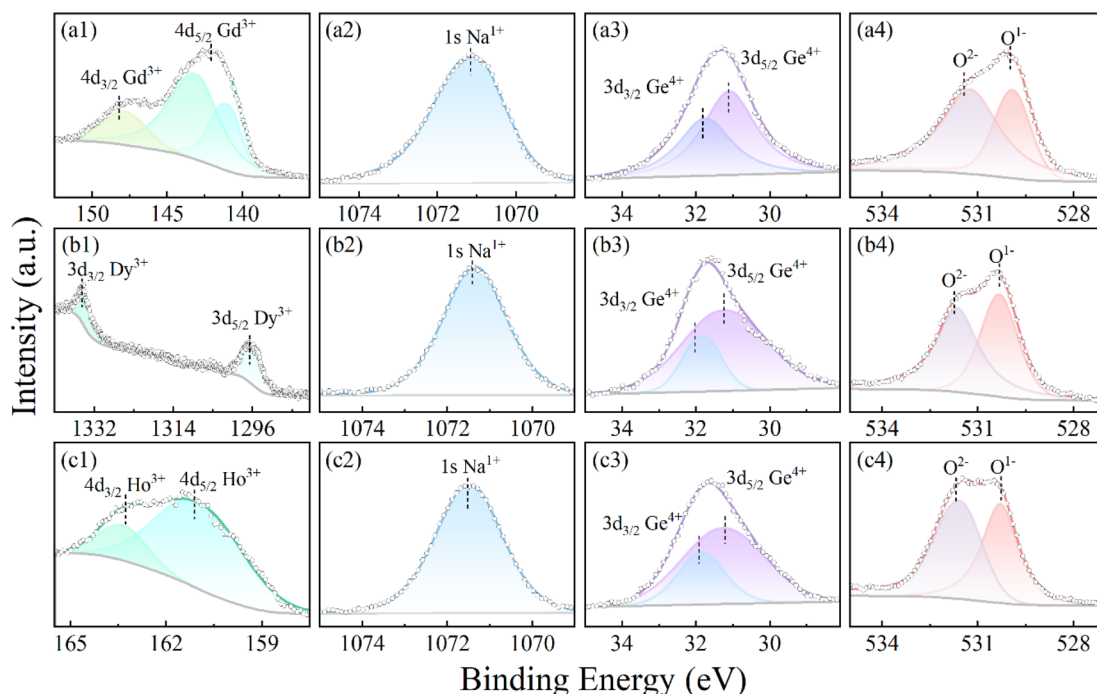


Fig. 4 XPS core-level spectra of constituent elements for (a)  $\text{GdNaGeO}_4$ , (b)  $\text{DyNaGeO}_4$ , and (c)  $\text{HoNaGeO}_4$  oxides.

[Fig. 3(a2)] are deduced to be 2.631 and 3.859 Å, typically corresponding to its [410] and [111] diffraction planes, respectively. The plane spacings of DyNaGeO<sub>4</sub> [Fig. 3(b2)] and HoNaGeO<sub>4</sub> [Fig. 3(c2)] are deduced to be 3.137 and 2.970 Å, typically corresponding to their [301] and [400] diffraction planes, respectively. In addition, the observed clear ring shape in SAED patterns [Fig. 3(a3)–(c3)] of these RENaGeO<sub>4</sub> oxides corresponding to the lattice planes are determined as follows: (524), (314), (102), (211) and (210) for GdNaGeO<sub>4</sub> oxide [Fig. 3(a3)]; (724), (342), (141), (222), (301) and (111) for DyNaGeO<sub>4</sub> oxide [Fig. 3(b3)]; and (024), (431), (331), (402) and (002) for HoNaGeO<sub>4</sub> oxide [Fig. 3(c3)], respectively. The TEM-EDS mapping analysis of Gd/Dy/Ho [Fig. 3(a4)–(c4)], Na [Fig. 3(a5)–(c5)], Ge [Fig. 3(a6)–(c6)] and O [Fig. 3(a7)–(c7)] indicate the uniform distribution of all the constituent elements in RENaGeO<sub>4</sub> oxides up to the nanoscale without notable segregations. Thus, these results reaffirm the single-phase character of these RENaGeO<sub>4</sub> oxides with good homogeneity.

The chemical valence states of RE (Gd, Dy, and Ho), Na, Ge and O in RENaGeO<sub>4</sub> oxides were assessed using XPS at RT. The XPS spectra reveal distinct signals for C (reference), Gd/Dy/Ho, Na, Ge and O elements, which align well with those obtained from TEM-EDS analysis. The high-resolution core-level XPS spectra of Gd/Ho-4d, Dy-3d, Na-1s, Ge-3d, and O-1s in GdNaGeO<sub>4</sub>, DyNaGeO<sub>4</sub>, and HoNaGeO<sub>4</sub> oxides and the corresponding peak-fitting results are illustrated in Fig. 4(a)–(c) respectively. The XPS core-level spectra of Gd-4d [Fig. 4(a1)], Dy-3d [Fig. 4(b1)] and Ho-4d [Fig. 4(c1)] all reveal two characteristic peaks located at 142.03 and 148.16 eV for GdNaGeO<sub>4</sub> oxide, at 1334.75 and 1296.53 eV for DyNaGeO<sub>4</sub> oxide, and at 163.28 and 161.12 eV for HoNaGeO<sub>4</sub> oxide, respectively, indicating the presence of Gd<sup>3+</sup>, Dy<sup>3+</sup> and Ho<sup>3+</sup> valence states. The core-level XPS spectra of Na-1s [Fig. 4(a2), (b2), and (c2)] in RENaGeO<sub>4</sub> oxides reveal a single character peak located around 1071.17 eV, indicating the presence of the Na<sup>1+</sup> valence state. In the XPS spectra of Ge-2p core-level [Fig. 4(a3), (b3), and (c3)] in RENaGeO<sub>4</sub> oxides, two characteristic peaks at around 32.03 and 31.23 eV corresponding to spin-orbit splitting of Ge-3d<sub>3/2</sub> and

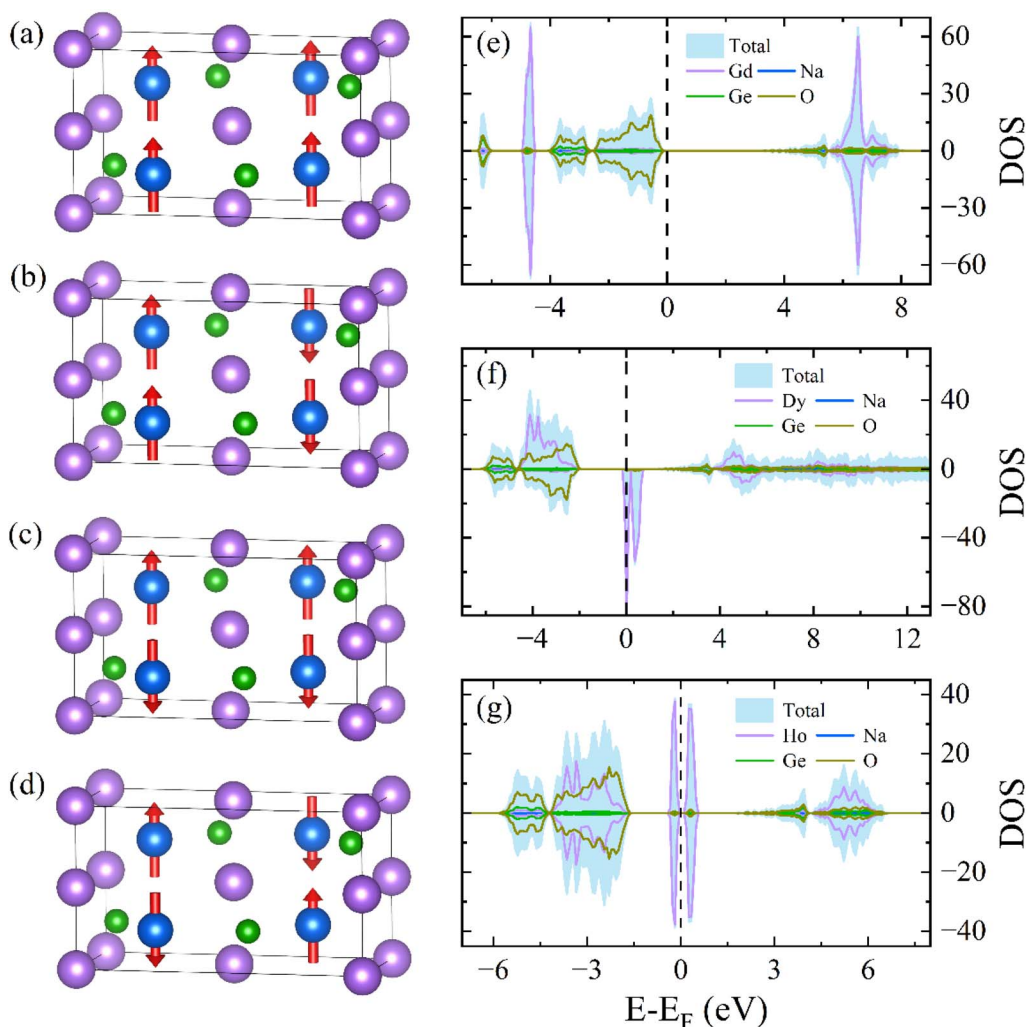


Fig. 5 Potential magnetic coupling of (a) FM and (b–d) AFM in RENaGeO<sub>4</sub> oxides. Spin-polarized total and partial DOS of (e) GdNaGeO<sub>4</sub>, (f) DyNaGeO<sub>4</sub>, and (g) HoNaGeO<sub>4</sub> oxides.

Ge-3d<sub>5/2</sub> can be noted, indicating the presence of Ge<sup>4+</sup> valence state. Additionally, the XPS spectra of the O-1s core level [Fig. 4(a4), (b4), and (c4)] in RENaGeO<sub>4</sub> oxides reveal two typical peaks at 529.98 and 531.43 eV, corresponding to the characteristic peak of O<sup>2-</sup> ions in the lattices and OH<sup>-</sup> on the surface, respectively.

To assess the ground-state magnetic and electronic properties of these RENaGeO<sub>4</sub> oxides, we performed spin-polarized first-principles DFT calculations<sup>37-39</sup> using commercial VASP software with PAW pseudopotentials.<sup>37-39</sup> We first evaluated the magnetic ground state of RENaGeO<sub>4</sub> oxides by calculating the total energy ( $E_{\text{tot}}$ ) for various potential spin configurations. Parallel (FM) and three anti-parallel (AFM: AFM1, AFM2, and AFM3) states are considered, as illustrated in Fig. 5(a)-(d). The calculated  $E_{\text{tot}}$  values of  $E_{\text{FM}}$ ,  $E_{\text{AFM1}}$ ,  $E_{\text{AFM2}}$  and  $E_{\text{AFM3}}$  are as follows: -226.7264, -226.7270, -226.7299 and -226.7297 eV per f.u. for GdNaGeO<sub>4</sub>; -210.3734, -210.3046, -210.3331 and -210.3344 eV per f.u. for DyNaGeO<sub>4</sub>; and -204.3413, -203.9209, -204.3958 and -204.2425 eV per f.u. for HoNaGeO<sub>4</sub>, respectively. Notably, the AFM2, FM and AFM2 states have the lowest  $E_{\text{tot}}$  in GdNaGeO<sub>4</sub>, DyNaGeO<sub>4</sub> and HoNaGeO<sub>4</sub>, respectively, illustrating that the AFM ground state is preferred for GdNaGeO<sub>4</sub> and HoNaGeO<sub>4</sub> oxides, whereas the FM ground state is preferred for DyNaGeO<sub>4</sub> oxide. Furthermore, we calculated the spin-polarized total density of states (DOS) and projected-orbital partial DOS for Gd(4f), Dy(4f), Ho(4f), Na(3s), Ge(4p), and O(2p) orbitals to further assess their electronic and magnetic characters, as illustrated in Fig. 5(e)-(g) for GdNaGeO<sub>4</sub>, DyNaGeO<sub>4</sub> and HoNaGeO<sub>4</sub>, respectively. Nearly identical states between spin-minority and spin-majority channels can be noted for GdNaGeO<sub>4</sub> and HoNaGeO<sub>4</sub> oxides with an evident band gap (BG) around the Fermi level, further proving their AFM ground state. However, the spin-minority and spin-majority channels in DyNaGeO<sub>4</sub> are asymmetric, indicating the possibility of an FM ground state. Additionally, the projected-orbital RE(4f) partial DOS predominantly governs the total DOS and exhibits significant splitting behavior in these RENaGeO<sub>4</sub> oxides, suggesting pronounced spontaneous polarization and large magnetic moments in RE<sup>3+</sup> ions. The calculated average magnetic moment of GdNaGeO<sub>4</sub> oxide is 6.88 $\mu_{\text{B}}$ , which is close to the theoretical limitation of a free Gd<sup>3+</sup> ion (7.0 $\mu_{\text{B}}$ ). However, the calculated average magnetic moments in DyNaGeO<sub>4</sub> and HoNaGeO<sub>4</sub> are 4.86 and 3.85 $\mu_{\text{B}}$ , respectively, which are only around half of the theoretical limit of the corresponding free RE<sup>3+</sup> ions. Such differences probably originate from the strong crystal field effects of Dy<sup>3+</sup> and Ho<sup>3+</sup> ions in RENaGeO<sub>4</sub> oxides.

The magnetic properties of RENaGeO<sub>4</sub> oxides were also experimentally determined with  $\mu_0H$  up to 7 T. The resulting  $M(T)$  and  $1/\chi(T)$  ( $\chi = M/\mu_0H$ ) curves of GdNaGeO<sub>4</sub>, DyNaGeO<sub>4</sub> and HoNaGeO<sub>4</sub> oxides under  $\mu_0H = 1$  T are illustrated in Fig. 6(a)-(c), respectively. Despite slight differences in values, these thermomagnetic results in RENaGeO<sub>4</sub> oxides exhibit similar behaviors: the values of  $M$  increase continuously as the temperature decreases, and the  $1/\chi(T)$  curves above 20 K of these RENaGeO<sub>4</sub> oxides follow a Curie Weiss law,  $\chi(T) = C/(T - \theta_p) + \chi_0$ , in which  $\theta_p$  and  $\chi_0$  represent paramagnetic Curie

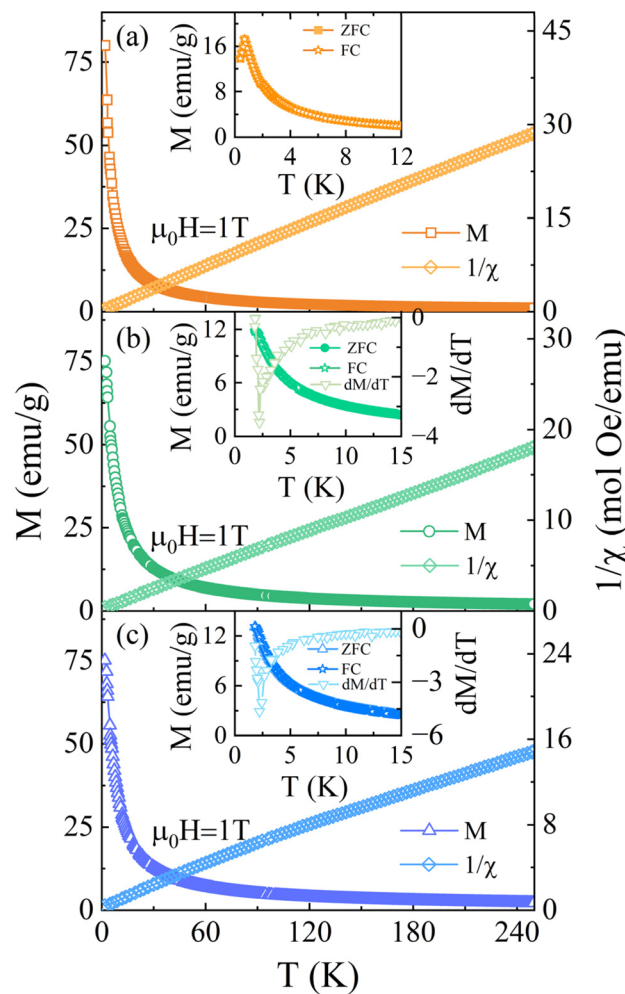


Fig. 6  $1/\chi(T)$  and  $M(T)$  curves under 1 T for (a) GdNaGeO<sub>4</sub>, (b) DyNaGeO<sub>4</sub>, and (c) HoNaGeO<sub>4</sub> oxides. Insets present corresponding FC, ZFC  $M(T)$  and  $dM/dT$  curves under 0.1 T.

temperature and temperature-independent part susceptibility, respectively. The Curie constant can be expressed as  $C = N(\mu_{\text{B}} - \mu_{\text{eff}})^2/3\kappa_{\text{B}}$ , where  $\mu_{\text{eff}}$  represents effective magnetic moment. The linear Curie Weiss fittings produce the  $\theta_p$  values of -0.36, 0.23 and -4.71 K for GdNaGeO<sub>4</sub>, DyNaGeO<sub>4</sub>, and HoNaGeO<sub>4</sub> oxides, respectively, indicating the possibility of ground state AFM interaction for GdNaGeO<sub>4</sub> and HoNaGeO<sub>4</sub> oxides, while FM interaction for DyNaGeO<sub>4</sub>, which aligns with those by DFT calculations. The corresponding deduced  $\mu_{\text{eff}}$  values for RENaGeO<sub>4</sub> oxides are 8.00, 10.58 and 10.62 $\mu_{\text{B}}$  per f.u., which align well with their respective theoretical magnetic moment of free RE<sup>3+</sup> ions, indicating the crucial roles of RE ions on magnetic properties in these RENaGeO<sub>4</sub> oxides. Additionally, the  $M(T)$  curves for these RENaGeO<sub>4</sub> oxides are illustrated in insets in Fig. 6(a)-(c) by FC and ZFC modes, which coincide within the experimental limitations, indicating the good thermal reversibility, which is demanded for magnetic refrigeration application. Moreover, the values of  $M$  in all RENaGeO<sub>4</sub> oxides increase gradually as temperature decreases to 1.8 K and show a saturation tendency for DyNaGeO<sub>4</sub> and HoNaGeO<sub>4</sub>.

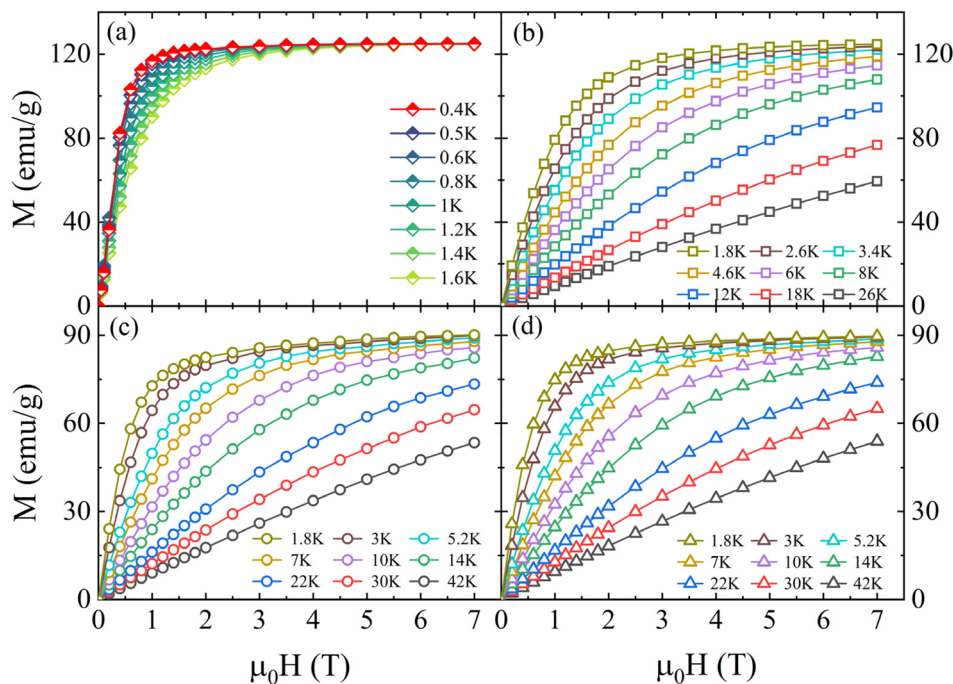


Fig. 7  $M(\mu_0 H)$  curves for (a and b)  $\text{GdNaGeO}_4$ , (c)  $\text{DyNaGeO}_4$ , and (d)  $\text{HoNaGeO}_4$  oxides.

oxides around 2 K, resulting in magnetic phase transition (MPT) temperatures of  $\sim 2.28$  and  $2.15$  K, respectively, based on the inflection point in their  $dM/dT(T)$  curves. However, the  $M$  value of  $\text{GdNaGeO}_4$  oxide increases continuously down to 1.8 K,

indicating no distinct magnetic ordering. Thus, we further determined the thermomagnetic results of  $\text{GdNaGeO}_4$  oxide down to 0.4 K using a dilute He-3 refrigerator, as illustrated in Fig. 6(a). A clear peak in the  $M(T)$  curves of  $\text{GdNaGeO}_4$  oxide can

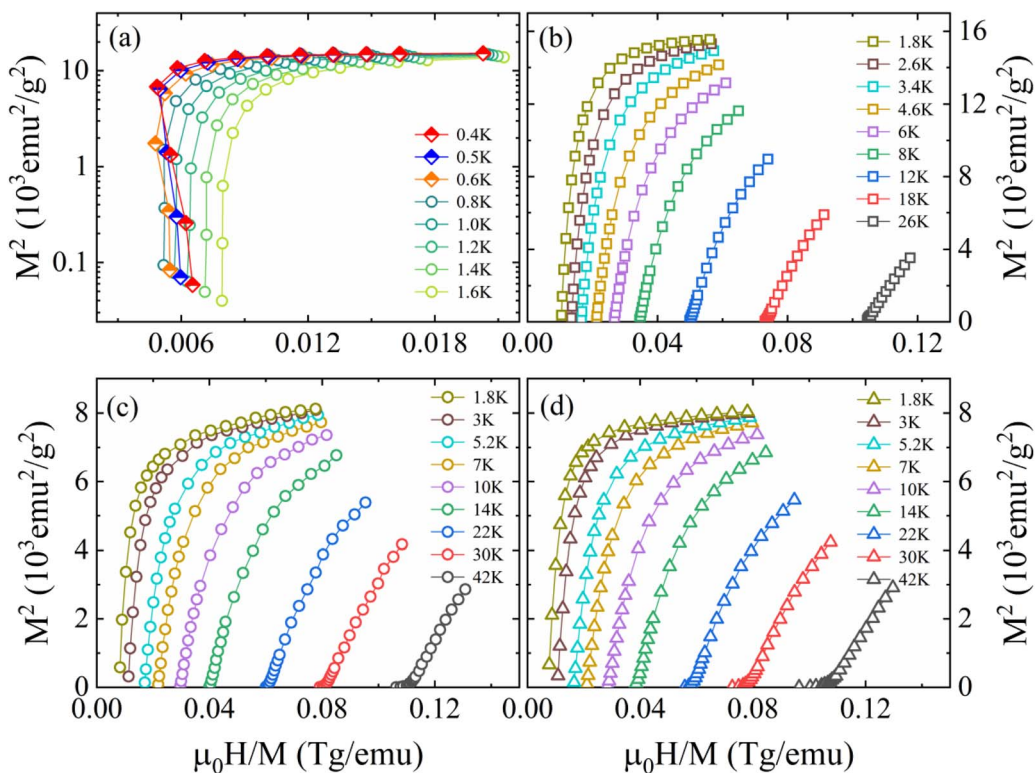


Fig. 8 Arrott-plot curves for (a and b)  $\text{GdNaGeO}_4$ , (c)  $\text{DyNaGeO}_4$ , and (d)  $\text{HoNaGeO}_4$  oxides.

be noted at around 0.7 K, indicating a typical MPT from the paramagnetic (PM) to AFM state.

Moreover, a series of  $M(\mu_0H)$  curves of  $\text{RENaGeO}_4$  oxides from 1.8 to 42 K (down to 0.4 K for  $\text{GdNaGeO}_4$ ) with  $\mu_0H$  up to 7 T were determined to further assess their MC responses and MPT nature, as illustrated in Fig. 7(a)–(d). Except for some differences in values, the  $M(\mu_0H)$  results of these  $\text{RENaGeO}_4$  oxides exhibit similar performances. Generally, the  $M$  values increase abruptly in the low-field region, then become flat, and finally show saturation behavior in the high-field region. MC performance is known to be proportional to the saturation magnetic moment ( $M_s$ ) of magnetic solids. The deduced  $M_s$  value for  $\text{GdNaGeO}_4$  reaches  $7.07\mu_B/\text{Gd}$  (0.4 K), which is close to the theoretical limitation of free  $\text{Gd}^{3+}$  ions; thus, notably low-temperature MC responses are expected. However, the  $M_s$  values are  $5.20\mu_B/\text{Dy}$  (1.8 K) and  $5.21\mu_B/\text{Ho}$  (1.8 K) for  $\text{DyNaGeO}_4$  and  $\text{HoNaGeO}_4$ , respectively, which are obviously lower than the theoretical values of the corresponding free  $\text{RE}^{3+}$  ions; such differences mainly originate from the strong crystal field effect and single-ion anisotropy for  $\text{Dy}^{3+}$  and  $\text{Ho}^{3+}$  ions. Additionally, these values align well with those obtained by the DFT calculations, further proving the vital roles of RE ions in the magnetism of these  $\text{RENaGeO}_4$  oxides. Moreover, the MC responses in solid-state magnets are related to their corresponding MPT order types,<sup>27–30</sup> which can be assessed by the slope signals in Arrott-plot ( $\mu_0H/M$  versus  $M^2$ ) curves, using the Banerjee criterion. The observation of a positive slope indicates the second-order type MPT,<sup>41</sup> while the exhibition of a negative slope corresponds to first-order type MPT.<sup>41</sup> Thus, to assess the order type of MPT in these  $\text{RENaGeO}_4$  oxides, the Arrott plot curves were transferred based on  $M(\mu_0H)$  results [Fig. 7(a)–(d)]. The resulting curves are correspondingly illustrated in Fig. 8(a)–(d), respectively. Clearly, negative slopes at low temperatures in  $\text{GdNaGeO}_4$  oxide [Fig. 8(a)] can be observed, illustrating the occurrence of first-order type MPT. However, only positive slopes are found for  $\text{DyNaGeO}_4$  and  $\text{HoNaGeO}_4$  oxides [Fig. 8(c)–(d)], indicating the second-order type MPT within the experimental limitations.

Subsequently, we first assessed the MC responses of these  $\text{RENaGeO}_4$  oxides using the temperature-dependent  $-\Delta S_M$ , evaluated using the equation

$$\Delta S_M(T, \Delta H) = \int_0^{H_{\max}} \left( \frac{\partial M(H, T)}{\partial T} \right)_H dH,$$

as illustrated in Fig. 9(a)–(c) for  $\text{GdNaGeO}_4$ ,  $\text{DyNaGeO}_4$ , and  $\text{HoNaGeO}_4$  oxides, respectively, which reveal a conventional MC response: only positive  $-\Delta S_M(T)$  values can be observed within the experimental limitations, and the value of  $-\Delta S_M$  under a fixed  $\Delta\mu_0H$  increases continuously with decreases in  $T$  and reaches its maximum ( $-\Delta S_M^{\max}$ ); after that,  $-\Delta S_M$  decreases gradually by further decreasing  $T$ . Under  $\Delta\mu_0H$  of 0–1, 0–2, 0–3, 0–5 and 0–7 T, the deduced  $-\Delta S_M^{\max}$  values are 22.22, 34.98, 40.90, 47.30 and 50.66 J (kg K)<sup>-1</sup> for  $\text{GdNaGeO}_4$ ; 7.15, 11.23, 13.00, 14.82 and 15.83 J (kg K)<sup>-1</sup> for  $\text{DyNaGeO}_4$ ; and 8.21, 12.21, 13.86, 15.37 and 16.22 J (kg K)<sup>-1</sup> for  $\text{HoNaGeO}_4$ , respectively. Evidently, the  $\text{GdNaGeO}_4$  possesses larger MC responses than those in  $\text{DyNaGeO}_4$  and  $\text{HoNaGeO}_4$  oxides, which is probably related to

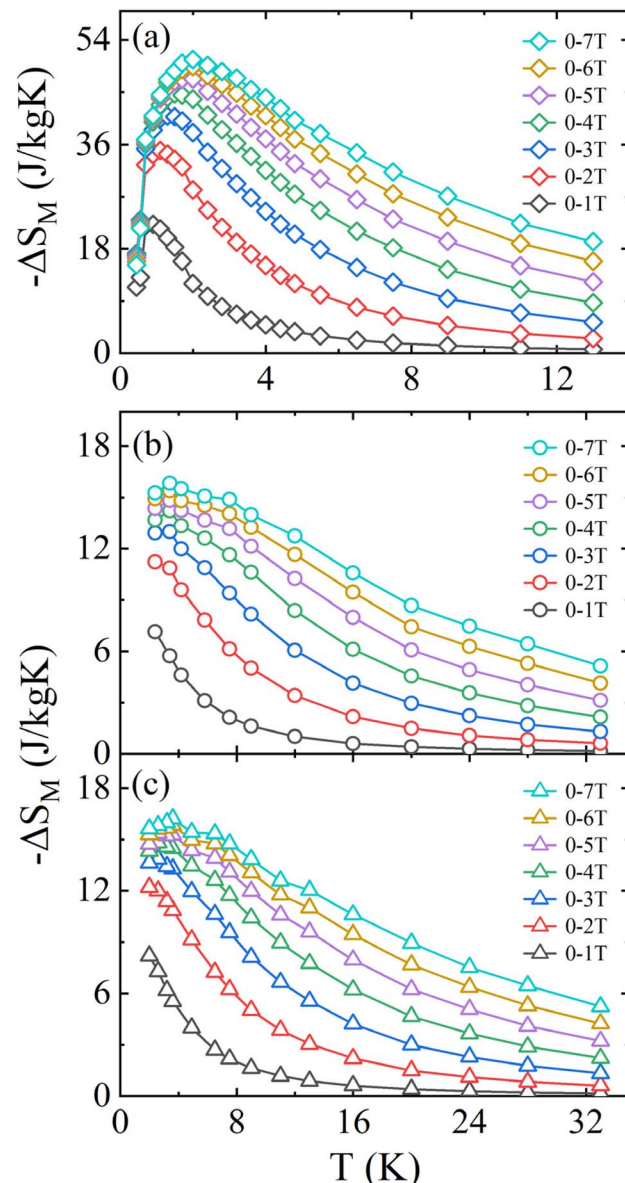


Fig. 9  $-\Delta S_M(T)$  curves for (a)  $\text{GdNaGeO}_4$ , (b)  $\text{DyNaGeO}_4$ , and (c)  $\text{HoNaGeO}_4$  oxides.

its low-field induced first order MPT and largest saturation magnetic moment with low crystal field effect. In addition, the values of refrigerant capacity ( $RC = \int_{T_{\text{cold}}}^{T_{\text{hot}}} |\Delta S_M(T)| dT$ ) and<sup>3–6</sup> relative cooling<sup>3–6</sup> power ( $RCP = |\Delta S_M^{\max}| \times \delta T_{\text{FWHM}}$ ) for  $\text{RENaGeO}_4$  oxides were deduced to further assess their MC responses. The  $T_{\text{cold}}$  and  $T_{\text{hot}}$  represent the temperatures at  $\frac{1}{2}|\Delta S_M^{\max}|$  in  $\Delta S_M(T)$  curves at two sides, and the  $\delta T_{\text{FWHM}}$  represents the absolute values of the difference between  $T_{\text{hot}}$  and  $T_{\text{cold}}$ . Consequently, the deduced  $RC(RCP)$  values under  $\Delta\mu_0H$  of 0–1, 0–2, 0–3, 0–5 and 0–7 T are as follows: 30.35(38.64), 82.87(107.56), 137.76(178.87), 245.53(320.70) and 351.46(462.10) J kg<sup>-1</sup> for  $\text{GdNaGeO}_4$ ; 21.23(28.73), 58.78(77.70), 100.02(130.92), 182.40(236.92) and 259.55(337.64) J kg<sup>-1</sup> for

**Table 1** Summary of  $T_M$  and  $-\Delta S_M^{\max}$  values of  $\text{GdNaGeO}_4$  oxide and selected low-temperature benchmarked MC materials

Materials	$T_M$ (K)	$-\Delta S_M^{\max}$ (0–2 T) $\text{J}(\text{kg K})^{-1}$	$-\Delta S_M^{\max}$ (0–5 T) $\text{J}(\text{kg K})^{-1}$	Ref.
$\text{GdNaGeO}_4$	0.7	34.98	47.30	Present
$\text{Gd}_3\text{Ga}_5\text{O}_{12}$	1.2	14.6	32.8	42 and 43
$\text{EuB}_2\text{O}_7$	0.7	36.2	47.6	44
$\text{Gd}_2\text{CuTiO}_6$	2.7	10.2	41.5	28
$\text{NaGdS}_2$	2.5	23.5	54	45
$\text{Gd}_{4.5}\text{K}_{0.5}\text{Si}_3\text{O}_{13}$	0.7	31.9	58.2	46
$\text{Gd}_3\text{TeBO}_9$	2.6	20.6	50.3	47
$\text{Gd}(\text{OH})\text{F}_2$	1.31	32	65	48
$\text{Gd}_{9.33}\text{Si}_6\text{O}_{26}$	0.65	32.5	59.5	49
$\text{Gd}_{152}\text{Ni}_{14}@\text{C}_{124}$	2.5	20.5	46	50

$\text{DyNaGeO}_4$ ; and 22.92(31.09), 61.66(81.18), 101.87(133.14), 183.25(239.47) and 262.50(345.20)  $\text{J kg}^{-1}$  for  $\text{HoNaGeO}_4$ , respectively. Evidently, the  $\text{GdNaGeO}_4$  oxide shows the best MC responses among the  $\text{RENaGeO}_4$  oxides, aligning with its larger saturation magnetic moment. Finally, to further identify the MC responses of  $\text{GdNaGeO}_4$  oxide, we summarize its  $-\Delta S_M^{\max}$  values under  $\Delta\mu_0H$  of 0–2 and 0–5 T with the reported benchmarked low-temperature MC materials, as illustrated in Table 1. The MC responses of the present  $\text{GdNaGeO}_4$  oxide under low  $\Delta\mu_0H$  of 0–5 T are comparable to most of the reported materials. Interestingly, its MC performance under low  $\Delta\mu_0H$  of 0–2 T, which could be generated by RE-dominated permanent magnets, is much larger than that of the commercialized MC material of  $\text{Gd}_3\text{Ga}_5\text{O}_{12}$  oxide and surpasses most of the benchmarked MC materials. Although  $-\Delta S_M^{\max}$  value under  $\Delta\mu_0H$  of 0–2 T is lower than that of the divalent Eu-based  $\text{EuB}_2\text{O}_7$  [44], the present  $\text{GdNaGeO}_4$  oxide has the benefit of being easy to fabricate by applying a simple solid-state reaction process with high environmental stability. These findings highlight  $\text{GdNaGeO}_4$  oxide as a top-level MC material that is attractive for practical low-temperature refrigeration applications.

## Conclusions

In summary, three single-phased  $\text{RENaGeO}_4$  oxides were successfully fabricated and unveiled their structural and magnetic properties, specifically for low-temperature MC responses through experimental determination and theoretical calculation. All these  $\text{RENaGeO}_4$  oxides crystallize in an Olivine-type orthorhombic structure and order magnetically at low temperatures of 0.7, 2.28 and 2.15 K for  $\text{GdNaGeO}_4$ ,  $\text{DyNaGeO}_4$ , and  $\text{HoNaGeO}_4$  oxides, respectively. The consistent elements in  $\text{NaREGeO}_4$  oxides are all distributed uniformly and present as  $\text{Na}^{1+}$ ,  $\text{RE}^{3+}$ ,  $\text{Ge}^{4+}$ , and  $\text{O}^{2-}$  valence states, respectively. Interestingly, the  $\text{GdNaGeO}_4$  oxide possesses remarkably low-temperature MC responses with the values of  $-\Delta S_M^{\max}$  reaching 22.22, 34.98, and 47.30  $\text{J}(\text{kg K})^{-1}$  under  $\Delta\mu_0H$  of 0–1, 0–2, and 0–5 T, respectively. These values, especially under low  $\Delta\mu_0H$  that can be generated by RE-dominated permanent magnets, are much larger than those of the commercial MC material of  $\text{Gd}_3\text{Ga}_5\text{O}_{12}$  oxide and surpass most of the updated benchmarked MC materials. These findings, in addition to their simple preparation process and high

environmental stability, make the  $\text{GdNaGeO}_4$  oxide an excellent candidate for low-temperature magnetic refrigeration applications.

## Data availability

The data supporting the findings of this study are available from the corresponding author, Yikun Zhang, upon reasonable request.

## Author contributions

Y. Z.: conceptualisation, supervision, project administration, resources, writing original draft, and review and editing; Y. N., Y. X., and X. Z.: investigation, formal analysis, and data curation. All authors have reviewed and approved the final version of the manuscript.

## Conflicts of interest

There are no conflicts to declare.

## Acknowledgements

This work was supported by the Zhejiang Provincial Natural Science Foundation of China (Grant No. LZ25E020002). The authors also acknowledge Dr Chao Zhang from the Instrumentation and Service Center for Physical Sciences at Westlake University for the magnetization measurements, and the Supercomputing Center of Hangzhou Dianzi University for providing computing resources.

## References

- 1 M. H. Phan and S. C. Yu, *J. Magn. Magn. Mater.*, 2007, **308**, 325–340.
- 2 O. Gutfleisch, M. A. Willard, E. Brück, C. H. Chen, S. G. Sankar and J. P. Liu, *Adv. Mater.*, 2011, **23**, 821–842.
- 3 V. Franco, J. Blázquez, J. Iplus, J. Law, L. Ramírez and A. Comde, *Prog. Mater. Sci.*, 2018, **93**, 112–232.
- 4 Y. Zhang, A. Li, W. Hao, H. F. Li and L. W. Li, *Acta Mater.*, 2025, **292**, 121033.

5 H. Zhong, Y. Song, F. Long, H. Lu, M. Ai, T. Li, Y. Yao, Y. Sakai, M. Ikeda, K. Takahashi, M. Azuma, F. Hu, X. Xing and J. Chen, *Adv. Mater.*, 2024, **36**, 2402046.

6 L. W. Li and M. Yan, *J. Mater. Sci. Technol.*, 2023, **136**, 1–12.

7 Y. Gong, X. Miao, F. Qian, F. Xu and L. Caron, *J. Phys. Condens. Matter*, 2024, **36**, 503001.

8 F. Zhang, X. Miao, N. van Dijk, E. Brück and Y. Ren, *Adv. Energy Mater.*, 2024, **14**, 2400369.

9 Y. Xie, Y. Na, F. Chen and Y. Zhang, *Inorg. Chem. Commun.*, 2025, **177**, 114395.

10 J. Lin, P. Tong, K. Zhang, W. Lu, X. Wang, X. Zhang, W. Song and Y. Sun, *Nat. Commun.*, 2022, **13**, 596.

11 (a) Y. Zhang, W. Hao, C. L. Hu, X. Wang, X. Zhang and L. Li, *Adv. Funct. Mater.*, 2023, **33**, 2310047; (b) W. Guo, X. Miao, J. Cui, S. Torii, F. Qian, Y. Bai, Z. Kou, J. Zha, Y. Shao, Y. Zhang, F. Xu and L. Caron, *Acta Mater.*, 2024, **263**, 119530.

12 F. Chen, Y. Na, Y. Xie and Y. K. Zhang, *ACS Appl. Mater. Interfaces*, 2024, **16**, 52719–52726.

13 Y. Song, J. Zhang, H. Li, H. Zhong, F. Long, Z. Wang, Y. Xu, X. Zheng, H. Zhang, Q. Huang, Y. Zhang, X. Xing and J. Chen, *Adv. Energy Mater.*, 2024, **14**, 2402527.

14 J. Wang, R. Ji, J. Xu, Z. Li, Y. Zhang and L. Li, *J. Magn. Magn. Mater.*, 2025, **619**, 172897.

15 Z. Li, A. Araujo, C. Roscini, J. G. Planas and E. Bartolomé, *J. Mater. Chem. A*, 2024, **12**, 21971–21986.

16 Y. Xie, L. F. Wang, Y. Z. Na and Y. Zhang, *J. Non-Cryst. Solids*, 2025, **658**, 123526.

17 F. Yang, J. Wang, R. Ji and Y. Zhang, *J. Electron. Mater.*, 2025, **54**, 4642–4647.

18 X. Tang, H. Sepehri-Amin, N. Terada, A. Martin-Cid, I. Kurniawan, Y. Kotani, H. Takeya, J. Lai, Y. Matsushita, T. Ohkubo, Y. Miura, T. Nakamura and K. Hono, *Nat. Commun.*, 2022, **13**, 1817.

19 Y. Zhang, J. Ying, X. Gao, Z. Mo, J. Shen and L. W. Li, *J. Mater. Sci. Technol.*, 2023, **159**, 163–169.

20 J. Ćwik, Y. Koshkid'ko, P. Putyra, B. Weise, M. Małecka, D. Gajda, M. Babij and A. Czernuszewicz, *Int. J. Hydrogen Energy*, 2024, **87**, 485.

21 J. Ćwik, Y. Koshkid'ko, K. Shinde, J. Park, N. A. de Oliveira, M. Babija and A. Czernuszewicz, *J. Mater. Chem. C*, 2024, **12**, 14421.

22 E. A. C. Koskelo, N. D. Kelly, L. A. V. Nagle-Cocco, J. D. Bocarsly, P. Mukherjee, C. Liu, Q. Zhang and S. E. Dutton, *Inorg. Chem.*, 2023, **62**, 10317–10328.

23 Y. K. Zhang, W. X. Hao, J. L. Lin, H. F. Li and L. W. Li, *Acta Mater.*, 2024, **272**, 119946.

24 J. Lin, S. Wu, K. Sun, H. F. Li, W. Chen, Y. Zhang and L. Li, *Ceram. Int.*, 2024, **50**, 51269–51277.

25 D. Wang, X. Zheng, L. He, H. Wu, Y. Gao, G. Wang, H. Liu, T. Pan, A. Ma, L. Xi, J. Xu, S. Wang and B. Shen, *Mater. Today Phys.*, 2025, **50**, 101609.

26 P. W. Doheny, J. Chen, T. Gruner, F. M. Grosche and P. J. Saines, *J. Mater. Chem. A*, 2023, **11**, 26474–26480.

27 Y. Zhang, W. Hao, J. Shen, Z. Mo, T. Gottschall and L. Li, *Acta Mater.*, 2024, **276**, 120128.

28 Y. K. Zhang, Y. Na, W. X. Hao, T. Gottschall and L. W. Li, *Adv. Funct. Mater.*, 2024, **34**, 2409061.

29 Y. K. Zhang, Y. Xie, J. J. Wei and W. X. Hao, *J. Mater. Chem. A*, 2024, **12**, 32396–32407.

30 W. Hao, R. Ji, L. Zhu, S. Huang and Y. Zhang, *Solid State Commun.*, 2025, **399**, 115876.

31 M. Emirdag-Eanes, M. Krawiec and J. W. Kolis, *J. Chem. Crystallogr.*, 2002, **31**, 281–285.

32 J. Yeon, J. B. Hardaway, A. S. Sefat, A. M. Latshaw and H. C. zur Loye, *Solid State Sci.*, 2014, **34**, 24–30.

33 X. Hou, T. Wan, D. Gao, X. Zhang, C. Jia, C. Du, R. Chai, Q. Pang, S. Yun and Y. Wang, *Mater. Today Chem.*, 2024, **39**, 102170.

34 Z. Liu, X. Yu, X. Yang, Q. Peng, X. Zhu, X. Xu and J. Qiu, *Inorg. Chem.*, 2023, **62**, 13362–13369.

35 X. Zhang, H. Song, R. Cui, K. Guo, M. Zhang and C. Deng, *Mater. Res. Bull.*, 2023, **167**, 112401.

36 L. Liu, K. Yu, L. Ming, Y. Sheng, S. Zheng, L. Song, J. Shi and Y. Zhang, *J. Rare Earths*, 2022, **40**, 1424–1431.

37 J. P. Perdew, K. Burke and M. Ernzerhof, *Phys. Rev. Lett.*, 1996, **77**, 3865.

38 G. Kresse and J. Furthmüller, *Phys. Rev. B*, 1996, **54**, 11169.

39 R. A. Evarestov and V. P. Smirnov, *Phys. Rev. B*, 2004, **70**, 233101.

40 J. Rodriguez-Carvajal, *FULLPROF: a Rietveld and Pattern Matching Analysis Program*, Laboratoire Leon Brillouin CEA-CNRS, France, 2007.

41 B. Banerjee, *Phys. Lett.*, 1964, **12**, 16–17.

42 A. C. S. Hamilton, G. I. Lampronti, S. E. Rowley and S. E. Dutton, *J. Phys.: Condens. Matter*, 2014, **26**, 116001.

43 M. Kleinhans, K. Eibensteiner, J. C. Leiner, C. Resch, L. Worch, M. A. Wilde, J. Spallek, A. Regnat and C. Pfleiderer, *Phys. Rev. Appl.*, 2023, **19**, 014038.

44 Y. Wang, J. Xiang, L. Zhang, J. Gong, W. Li, Z. Mo and J. Shen, *J. Am. Chem. Soc.*, 2024, **146**, 3315.

45 C. Delacotte, T. A. Pome洛va, T. Stephan, T. Guizouarn, S. Cordier, N. G. Naumov and P. Lemoine, *Chem. Mater.*, 2022, **34**, 1829.

46 Y. Zhang, J. Y. Law, A. Li, W. Hao, V. Franco and L. Li, *Small*, 2025, **21**, 2409981.

47 C. Q. Zhou and R. K. Li, *Chem.-Eur. J.*, 2024, **30**, 2303048.

48 Q. Xu, B. Liu, M. Ye, G. L. Zhuang, L. Long and L. Zheng, *J. Am. Chem. Soc.*, 2022, **144**, 13787.

49 Z. W. Yang, J. Zhang, B. Liu, X. Zhang, D. Lu, H. Zhao, M. Pi, H. Cui, Y. J. Zeng, Z. Pan, Y. Shen, S. Li and Y. W. Long, *Adv. Sci.*, 2024, **11**, 2306842.

50 N. Xu, W. Chen, Y. Ding and Z. Zheng, *J. Am. Chem. Soc.*, 2024, **146**, 9506–9511.